


Manipulating corner states without topological phase transition in two-dimensional intrinsic triferroic materials

Xiaoran Feng , Runhan Li, Zhiqi Chen, Ying Dai,^{*} Baibiao Huang, and Chengwang Niu [†]
School of Physics, State Key Laboratory of Crystal Materials, Shandong University, Jinan 250100, China

 (Received 30 January 2024; revised 9 April 2024; accepted 15 April 2024; published 30 April 2024)

Engineering topological boundary states have attracted enormous interest with great insight into both the fundamental understanding and future applications of topological states. Despite the fact that several proposals have been made to achieve the second-order corner states from the first-order helical and/or chiral edge states, manipulation of corner states without topological phase transition remain elusive. Here, taking γ -FeO₂H monolayer and 1T'-CrCoS₄ monolayer as the material candidates, we propose a general mechanism for manipulating corner states without topological phase transition in two-dimensional intrinsic triferroics. Under in-plane spontaneous polarization, electrons acquire a transverse velocity, leading to the emergence of nontrivial corner states located at the mirror-symmetric corners perpendicular to the polarization direction. Remarkably, in contrast to previously reported proposals with topological phase transition, we put forward that the spatial distribution of the corner states can be effectively engineered by a ferroelastic switching with the second-order topological insulator remaining intact, thereby driving the advancement of multiferroics in topological spintronics.

DOI: [10.1103/PhysRevB.109.165308](https://doi.org/10.1103/PhysRevB.109.165308)

I. INTRODUCTION

Recent advancements in topological states have greatly expanded the classification of band insulators, and remarkably, the nontrivial bulk-boundary correspondence reaches out to higher orders, namely, higher-order topological insulators (HOTIs) [1–3]. Unlike conventional TIs, HOTIs feature topologically gapless boundary states with a dimensionality lower by more than one compared to that of the bulk [2]. For example, the second-order topological insulators (SOTIs) host gapless states at the ($d-2$) dimensional boundaries, resulting in the hinge or corner states in three or two dimensions, respectively [4–8]. This characteristic enhances the prevalence of nondissipative states and paves the way for feasible transport signatures with potential applications in topotronic devices [9,10]. Numerous theoretical models and material candidates of SOTIs have been proposed [11–17], and they have been experimentally observed in Bi [18], WTe₂ [19], and Bi₄Br₄ [20]. Notably, in two-dimensional (2D) materials, the topology and nontrivial corner states can be engineered, such as the nontrivial corner states can be obtained when the magnetization directions are switched in topological crystalline insulators and/or when an in-plane Zeeman field is introduced in the Z₂ TIs [21–24]. However, despite the exciting progress, the corner states engineering is severely limited in the topological phase transitions, where indeed topological phase transitions between SOTIs and Chern insulators can also emerge [25,26].

On the other hand, multiferroic coupling in 2D materials gives rise to exotic effects with versatile capabilities for manipulating strain alignment, electric polarization, and magnetization [27–33]. Typical ferroic properties include ferromagnetism (FM)/antiferromagnetism (AFM) resulting

from the breaking of time-reversal symmetry, and ferroelectrics (FE)/ferroelastics (FA) that arise in the absence of certain structural symmetry [34–36]. Among various multiferroics, intrinsic triferroics, holding three simultaneous (anti)ferroic orders, are rare but highly sought after, providing an ideal platform for multistate information devices [32,37–40]. Remarkably, coupling multiferroic to nontrivial topological physics in 2D holds great promise for both fundamental research and applications in topotronics and nonvolatile memory devices [41–49]. Indeed, the interplay between band topology and ferroic properties allows for the topological phase transitions through elastic strain engineering or the direct control by an electric field [50–52]. Therefore, an outstanding question arises as to whether the corner states can be effectively tuned by multiferroic while remaining the SOTIs.

In the present work, we demonstrate that 2D intrinsic triferroics γ -FeO₂H monolayer and 1T'-CrCoS₄ monolayer provide a promising platform to achieve the SOTI phase, and remarkably to control the corner states without topological phase transition. With the ferroelectric polarization, nontrivial corner states arise in the mirror-symmetric corners, which can be demonstrated by the energy spectra in nanoflakes and the spatial charge distribution. Notably, under a ferroelastic switching from the initial to final stable states, the spatial distribution of the corner states undergoes a 90° rotation. Yet, during intermediary states of ferroelastic and ferroelectric switching, the corner states disappear. Our findings suggest that magnetic topological corner states can be engineered by ferroelasticity and ferroelectricity, offering a practical experimental approach for manipulating the topology in next-generation electronic devices.

II. METHODS

As implemented in the Vienna *ab initio* simulation package (VASP), the projector-augmented wave method is used

^{*}daiy60@sdu.edu.cn

[†]c.niu@sdu.edu.cn

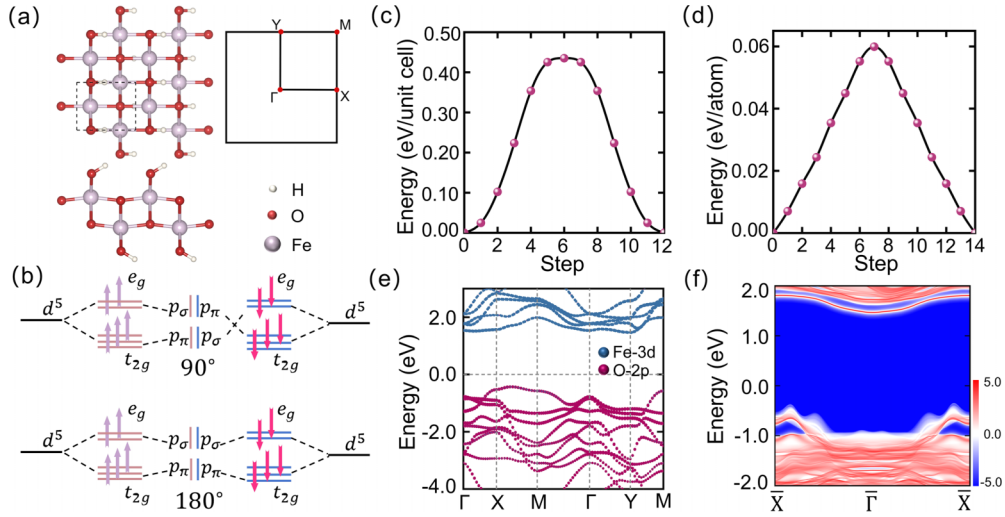


FIG. 1. (a) Top and side views of the γ -FeO₂H monolayer with the unit cell is indicated by dashed lines, and the corresponding 2D Brillouin zone. (b) Diagrammatic depiction of the super exchange paths in the γ -FeO₂H monolayer, where dashed lines indicate electron transitions between orbitals. Energy pathway for (c) ferroelectric switching and (d) ferroelastic switching as a function of step number in the nudged elastic band calculations. (e) Orbitaly resolved band structure with SOC and (f) edge state for γ -FeO₂H monolayer in the initial stable state of ferroelectric/ferroelastic switching. The band structure is orbitaly weighted with the contributions of Fe-3d and O-2p states.

to perform the first-principles calculations based on density functional theory [53,54]. The generalized gradient approximation (GGA) of Perdew-Burke-Ernzerhof (PBE) is used for the exchange-correlation potential [55]. The plane-wave cutoff energy is set at 450 eV and the Brillouin zone is sampled using a $11 \times 11 \times 1$ Γ -centered k -point mesh. A vacuum layer of 20 Å is used to avoid interactions between the nearest slabs. During structural optimization, we fully relax both the atomic positions and lattice constants of each system until the Hellmann-Feynman forces acting on each atom are below 0.01 eV/Å. The electronic convergence criteria is set to 10^{-5} eV. For the Fe-3d, Cr-3d, and Co-3d electrons, the GGA + U method with values of 4.3 eV, 2.2 eV, and 2 eV are used to correct the Coulomb interactions [56,57]. The ferroelastic transition pathway and the energy barrier are calculated using the NEB method. The maximally localized Wannier functions (MLWFs) are constructed using the WANNIER90 code [58].

III. RESULTS AND DISCUSSION

Recently, the γ -FeO₂H monolayer has attracted growing interest as an intrinsically 2D triferroic semiconductor [56]. An atomically thin γ -FeO₂H nanosheet, approximately 1.5 nm thick, has been experimentally synthesized [59], and the stability of the γ -FeO₂H monolayer has been confirmed through phonon spectra, elastic constants, and AIMD simulations [56]. Figure 1(a) presents the top and side views of the γ -FeO₂H monolayer. It belongs to the noncentrosymmetric space group $Pmn2_1(C_{2v})$, with a rectangular unit cell containing two Fe atoms, two H atoms, and four O atoms. The optimized lattice constants of the γ -FeO₂H monolayer are $a = 3.81\text{Å}$ and $b = 3.09\text{Å}$, in agreement with previous calculations [56].

Each Fe atom is coordinated by six O atoms in a distorted octahedral environment, and thus the Fe-3d orbitals

split into the double-degenerate e_g and triple-degenerate t_{2g} orbitals as depicted in Fig. 1(b). The calculations of magnetic properties reveal that the magnetic moments on each Fe are about $5 \mu_B$, suggesting that the Fe are in a high-spin state with the half filled $3d^5$ configuration, giving rise to the intrinsic antiferromagnetism. To further verify the magnetic ground state, we calculated the total energies of four different magnetic configurations with spin polarization, including three antiferromagnetic (AFM) states and one ferromagnetic (FM) state (see Fig. S1 in the Supplemental Material [60]). The AFM-1 is identified as the ground state, which is energetically lower than the AFM-2, AFM-3, and FM states by 0.06, 0.05, and 0.11 eV/atom, respectively. The origin of such ground AFM-1 configuration in the γ -FeO₂H monolayer can be elucidated through the superexchange interaction following the Goodenough-Kanamori-Anderson rules [61,62]. As illustrated in Fig. 1(b), through the O-2p orbitals between Fe, magnetic moments from spin-polarized e_g and t_{2g} states couple antiferromagnetically in different paths based on the Fe-O-Fe angle, i.e., the $e_g - p_\sigma/p_\pi - t_{2g}$ path with a 90° angle, and/or $e_g - p_\sigma/p_\sigma - e_g$ and $t_{2g} - p_\pi/p_\pi - t_{2g}$ path with a 180° angle [61,62]. The intensity of the antiferromagnetic coupling for the 90° case is weaker than that for the 180° case [62]. For γ -FeO₂H monolayer, the Fe-O-Fe angle along the [100] direction is closer to 180° , while those are closer to 90° along the [010] and [110] directions, suggesting the strong antiferromagnetic coupling along the [100] direction. Additionally, Figs. 1(c) and 1(d) display the energy pathways for ferroelectric switching and ferroelastic switching, respectively, as a function of step number in the nudged elastic band calculations for the γ -FeO₂H monolayer. The energy barrier for the ferroelectric switching is estimated to be 0.44 eV/unit cell, and that for the ferroelastic switching is estimated to be 0.058 eV/atom, suggesting a high possibility of both the ferroelectric switching and ferroelastic switching in the γ -FeO₂H monolayer.

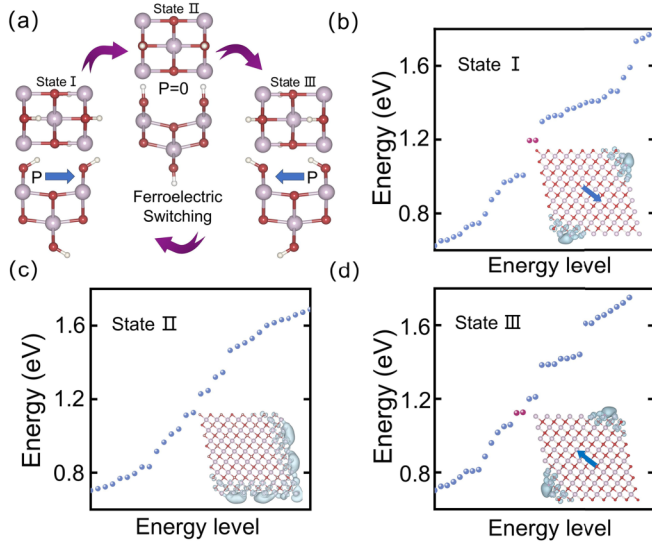


FIG. 2. (a) Schematic diagram of ferroelectric switching for the γ -FeO₂H monolayer. Energy discrete spectrums for the (b) initial state (state I), (c) intermediate state (state II), and (d) final state (state III) of the ferroelectric switching for γ -FeO₂H nanoflakes. The charge distributions of corner states and/or edge states are plotted in the insets. The magenta dots represent the in-gap corner states. Blue arrows represent the directions of spontaneous in-plane polarization.

To get preliminary insight into the topological properties of the γ -FeO₂H monolayer, we calculate the band structure without and with SOC, and present in Fig. 1(e) the orbitally resolved band structures with SOC. Clearly, the γ -FeO₂H monolayer is an AFM semiconductor with an indirect band gap of 2.32 eV. The conduction band minimum (CBM) is dominated by the $3d$ orbitals of Fe, whereas the valence band maximum (VBM) is mainly derived from the $2p$ orbitals of O. There is no SOC-induced band inversion that is usually considered as a heuristic scenario for the conventional Z_2 TIs. Moreover, calculations of the edge Green's function of a semi-infinite γ -FeO₂H nanoribbon are carried out by using the iterative method and the MLWFs, and the resulting local density of states are illustrated in Fig. 1(f). Obviously, there is a large gap between the conduction and valence bands, and no gapless edge states appear in the bulk band gap. Thus, the γ -FeO₂H monolayer is not a 2D Z_2 TI. However, the floating edge states appear in the bulk band gap, which is usually considered as an important signature of the SOTIs.

Concerning the space group $Pmn2_1(C_{2v})$, only the M_y mirror symmetry exists. The absence of M_x mirror symmetry in the γ -FeO₂H monolayer is due to the O-H bond deviating from the c axis by a maximum angle of $\theta_{\max} = 60.5^\circ$, as shown in state I of Fig. 2(a). It is noteworthy that this deviation induces in-plane polarizations of ferroelectricity in the γ -FeO₂H, leading to the emergence of corner states, another important hallmark of the SOTIs. To explore the SOTIs phase, we perform calculations of the energy discrete spectra and charge spatial distribution for a $4\sqrt{2} \times 4\sqrt{2}$ γ -FeO₂H nanoflake. Figure 2(b) displays the energy spectra of the nanoflake in state I, i.e., the initial state for the ferroelectric switching, where two clearly visible degenerate in-gap states

are obtained. In particular, the spatial distribution of these corner states is well localized at the corners, revealing explicitly the 2D SOTIs character of the γ -FeO₂H monolayer.

The unique coexistence of excellent ferroelectricity and band topology provides extraordinary platforms for realizing multipurpose and controllable devices. Figure 2(a) presents the top and side views for the initial, intermediate, and final states of the ferroelectric switching for the γ -FeO₂H monolayer, marked as state I, state II, and state III, respectively. As shown in Fig. 1(c), the transition pathway is symmetrical. Similar to reported ferroelectric materials, the intermediate state of the γ -FeO₂H monolayer is metastable, where the phonon dispersions host imaginary modes in the Brillouin zone. The O-H bonds are aligned parallel to the c axis, there is the structural inversion symmetry for the intermediate state II, and thus no spontaneous polarization. At the same time, there is no corner state distribution in the finite nanoflake as illustrated in Fig. 2(c). By rotating the angle between the O-H bond and the c axis from θ_{\max} to $-\theta_{\max}$, we achieve the final ferroelectric state, state III of Fig. 2(a). The spontaneous polarization is obtained again. The emergence of the in-gap corner states for final state III is clearly visible, as depicted in Fig. 2(d), and the spatial distribution of corner states is well localized at the corners, indicating that the ferroelectricity with in-plane polarizations endows the emergence of corner states in the γ -FeO₂H monolayer. However, for both state I and state III, the corner states emerge only at the top right and bottom left corners, but not at the top left and bottom right corners, as shown in the insets of Figs. 2(b) and 2(d). This is due to the fact that distribution of corner states is related to the orientations of spontaneous ferroelectric polarization. Electrons within the materials experience deflection as a result of the combined effects of spontaneous in-plane polarization and Berry curvature, described as $v(\mathbf{k}) = A\mathbf{E} \times \Omega(\mathbf{k})$ [63]. Here, A is a constant, E signifies the spontaneous polarization, and $\Omega(\mathbf{k})$ represents the Berry curvature. A velocity $v(\mathbf{k})$ perpendicular to the orientations of spontaneous in-plane polarization field is obtained, leading to the accumulation of corner charges for state I and state III as shown in Figs. 2(b) and 2(d).

Notably, for multiferroic materials with the coexistence of ferroelectricity and ferroelasticity, the directions of spontaneous ferroelectric polarization can be further switched via the ferroelastic transition. Due to different lattice constants on the a and b axes, the γ -FeO₂H monolayer has two stable states, F and F' , with a transition state, TS , which are the initial, final, and intermediate states of the ferroelastic switching, respectively, as illustrated in Fig. 3(a). Clearly, the crystal structure for the F state is the same as that of the F' state rotated by 90° , where the lattice constant a of the F state is larger than b , while a is smaller than b for the F' state. When subjected to external in-plane strain, the F state and the F' state of γ -FeO₂H can undergo reversible phase transitions. As a consequence, the ferroelastic switching causes a 90° rotation in the directions of the spontaneous ferroelectric polarization for the γ -FeO₂H monolayer.

To better illustrate how the ferroelastic switching controls the corner states, we set its initial state, F state, to be the same as the initial state, state I, of the ferroelectric transition. For the TS and F' states of the ferroelastic transition, we con-

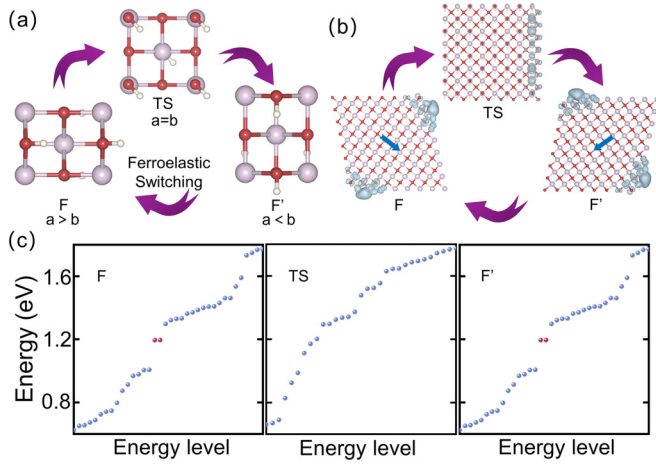


FIG. 3. (a) Schematic diagram of ferroelastic switching for the γ -FeO₂H monolayer. (b) Charge distributions of corner states and/or edge states for the ferroelastic initial state (F), transition state (TS), and final state (F') of the γ -FeO₂H monolayer; the blue arrows represents the directions of spontaneous in-plane polarization. (c) Energy discrete spectra of the γ -FeO₂H nanoflakes under states F , TS , and F' . The magenta dots in states F and F' signify the in-gap corner states.

struct the corresponding $4\sqrt{2} \times 4\sqrt{2}$ nanoflakes and calculate the energy discrete spectra and charge spatial distribution, and present the obtained results in Figs. 3(b) and 3(c). As discussed above, for the initial F state, the corner states emerge at the top right and bottom left corners. And for the intermediate TS state, with $a = b$, the spontaneous polarization vanishes, resulting in the charges distributes no longer at the corners but along the edge of the nanoflake. Remarkably, for the final F' state, the energy spectra behave exactly the same as that of the another ferroelastic ground state F . However,

the spatial distribution of their corner states is very different, rotating by 90° , i.e., emerging at the top left and bottom right corners for the F' state. One can thus safely recognize the feasibility of tuning the spatial distribution of corner states via ferroelastic transition.

We then calculate the reversible ferroelastic strain of the γ -FeO₂H monolayer to gain a deeper understanding of the ferroelastic switching. This strain controls the signal strength, defined as $|a/b - 1| \times 100\%$. The obtained reversible ferroelastic strain for the γ -FeO₂H monolayer is 23.30%, on par with those of GeS (17.8%), Nb₂GeTe₄ (22.1%), and Nb₄SiTe₄ (24.4%), indicating a strong switching signal [64,65]. Hence, ferroelastic switching can be effectively used to engineer the corner states in the γ -FeO₂H monolayer, leading to a plethora of intriguing phenomena and potential applications.

At last, we explore and show the emergence and engineering of corner states with the same mechanism can indeed be realized in other 2D intrinsic triferroic materials, such as the 1T'-CrCoS₄ monolayer. Figure 4(a) displays the top and side views of the 1T'-CrCoS₄ monolayer. It is evident that the reduced C_3 symmetry in 1T'-CrCoS₄ results in a spontaneous in-plane polarization with a value of $0.86 \times 10^{-4} \mu\text{C}/\text{m}$ [57]. The optimized lattice constants for the 1T'-CrCoS₄ monolayer are $a = 5.38\text{\AA}$ and $b = 3.22\text{\AA}$. The ground state displays a ferrimagnetism order with antiparallel spin alignment between Cr and Co atoms, and a net magnetic moment of $1.00 \mu_B/\text{unit cell}$.

Figure 4(b) presents the orbitally resolved band structures of the 1T'-CrCoS₄ monolayer with SOC. It is an indirect semiconductor with a bandgap of 0.22 eV, and the valence and conduction bands near the Fermi level are mainly contributed by the S-3p, Cr-3d, and Co-3d orbitals. Top views of initial state F , transition state TS , and final state F' for the ferroelastic switching of the 1T'-CrCoS₄ monolayer are displayed in Fig. 4(d). To explicitly uncover the SOTIs nature with tunable

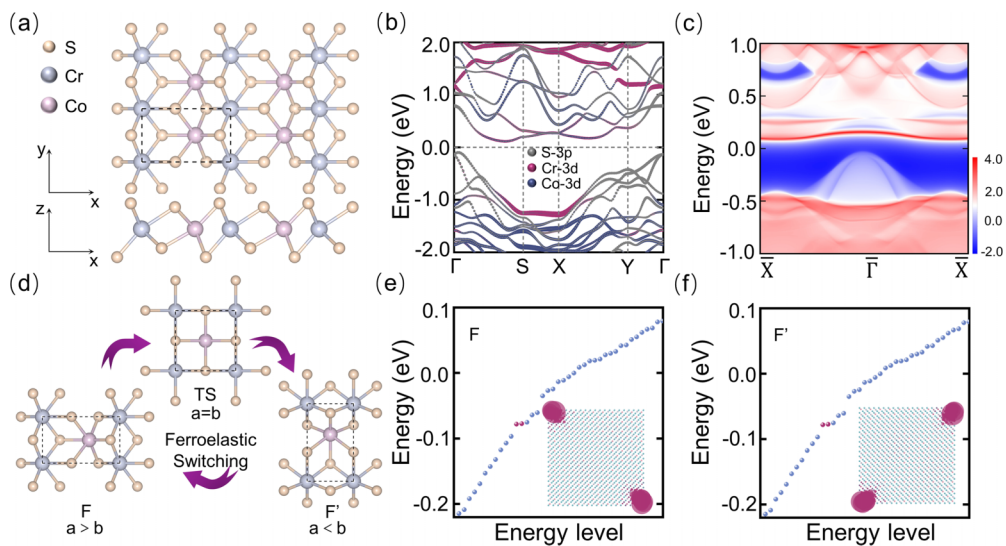


FIG. 4. (a) Top and side views of the 1T'-CrCoS₄ monolayer with the unit cell is indicated by dashed lines. (b) Orbitally resolved band structure with SOC and (c) edge state for 1T'-CrCoS₄ in the initial stable state of ferroelastic switching. The band structure is orbitally weighted with the contributions of S-3p, Cr-3d, and Co-3d states. (d) Schematic diagram of ferroelastic switching for the 1T'-CrCoS₄ monolayer. Energy-discrete spectra of the 1T'-CrCoS₄ nanoflake for (e) initial state (F) and (f) final state (F') associated with the ferroelastic switching. The magenta dots represent the in-gap corner states with their distributions displayed in the corresponding insets.

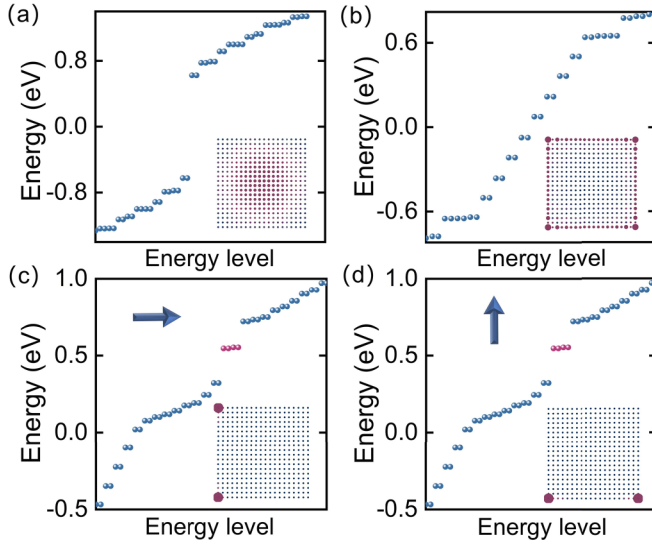


FIG. 5. Energy spectrum of finite nanoflakes for the TB model under (a) trivial ($m = 2.5, F = 0$), (b) nontrivial ($m = 0.5, F = 0$), and (c), (d) higher-order phases with in-plane electric polarization ($m = 0.5, F = 1.3$). The parameters t and λ are set to 0.5 and 0.2, respectively. The magenta dots represent the in-gap corner states, the blue arrow denotes the direction of the electric potential, and the distributions of corner, edge, and bulk states are plotted in the inset.

corner states, calculations of edge states of a semi-infinite nanoribbon are carried out using MLWFs constructed based on the Cr-3d, Co-3d, and S-3p orbitals. Similar to γ -FeO₂H, as shown in Fig. 4(c), floating edge states emerge in the bulk band gap. Then, we used MLWFs to construct 0D nanoflakes, and studied both the energy spectrum and the spatial distribution of corner states, as depicted in Figs. 4(e) and 4(f) for F and F' states, respectively. Obviously, one can see that the corner states are well localized at the corners and are oriented perpendicular to the in-plane spontaneous polarization directions. Furthermore, as depicted in the insets of Figs. 4(e) and 4(f), the localization of corner states rotates 90° for two stable ferroelastic states F and F' , which is in direct agreement with the above discussed γ -FeO₂H monolayer.

Finally, to better grasp the key mechanisms and physics of the switchable corner states, we present a tight-binding model, where each primitive cell includes one atom with two orbitals. The corresponding Hamiltonian can be expressed as

$$H_0 = -t \sum_{\langle i,j \rangle} c_i^\dagger c_j + \sum_i m_i c_i^\dagger c_i + \lambda \sum_{\langle i,j \rangle \alpha \beta} c_{i\alpha}^\dagger (\sigma_{\alpha\beta} \cdot d_{ij}) c_{j\beta},$$

where $c_{i\alpha}^\dagger$ ($c_{i\beta}$) annihilates (creates) an electron in the position i , with a spin component of α (β), and d_{ij} is the vector connecting the two atoms. The first term represents the nearest-neighbor hopping with energy t , while the second

term is the onsite sublattice potential, where $m_i = \pm m$ for the s and p orbitals, respectively. The third term represents the nearest-neighbor spin-orbit coupling (SOC) with amplitude λ , inducing hybridization between s - s or p - p orbitals. As shown in Figs. 5(a) and 5(b), the system can be either a normal insulator or a 2D Z_2 TI, but not a 2D SOTI due to the lacking of polarization in the presence of rotation symmetries C_{2x} and C_{2y} .

To mimic the polarization, we then introduce the electric potential term $H_E = \sum_i c_i^\dagger [eF(x \cos \theta + y \sin \theta)] c_i$. In addition to the elementary charge e , H_E is characterized by the amplitude represented by F and orientation defined by θ . As expected, with an in-plane electric potential along the \hat{x} direction, four clearly degenerate states emerge within the band gap as depicted in Fig. 5(c). The spatial distribution of wave functions for these energy states is well localized at two symmetric corners on the lower side of the electric potential, serving as a direct signal of 2D SOTIs. Remarkably, the in-gap corner states can be relocated when considering the in-plane electric potential along the \hat{y} direction, as depicted in Fig. 5(d). Given the coexistence of ferroelectricity and ferroelasticity in multiferroic materials, the direction of spontaneous ferroelectric polarization can be switched through ferroelastic transitions. Consequently, controlling the corner states via ferroelastic transitions becomes not only conceivable but also elegantly feasible.

IV. CONCLUSIONS

In summary, we successfully confirmed that the SOTI phase with corner states can emerge in the 2D intrinsic tri-ferroics γ -FeO₂H monolayer and 1T'-CrCoS₄ monolayer, and remarkably the corner states can be effectively modulated by the ferroelastic and ferroelectric switchings. The emergence of corner states stems from the intrinsic spontaneous ferroelectric polarization, which are located at mirror-symmetric corners perpendicular to the in-plane spontaneous polarization direction, and disappear with the vanishing of the ferroelectric polarization. Moreover, given the ferroelastic transition from the initial to final stable states, the localization-control of corner states can be achieved via ferroelastic switching due to the changing of directions of the in-plane spontaneous polarization. Our findings greatly enrich the prominent fundamental phenomena and thus provide an outstanding avenue for designing novel controllable topotronic devices.

ACKNOWLEDGMENTS

This work was supported by the National Natural Science Foundation of China (Grants No. 12174220 and No. 12074217), the Shandong Provincial Science Foundation for Excellent Young Scholars (Grant No. ZR2023YQ001), the Taishan Young Scholar Program of Shandong Province, and the Qilu Young Scholar Program of Shandong University.

- [1] W. A. Benalcazar, B. A. Bernevig, and T. L. Hughes, *Science* **357**, 61 (2017).
- [2] F. Schindler, A. M. Cook, M. G. Vergniory, Z. Wang, S. S. Parkin, B. A. Bernevig, and T. Neupert, *Sci. Adv.* **4**, eaaf0346 (2018).

- [3] J. Xiao and B. Yan, *Nat. Rev. Phys.* **3**, 283 (2021).
- [4] Q. Wang, C.-C. Liu, Y.-M. Lu, and F. Zhang, *Phys. Rev. Lett.* **121**, 186801 (2018).
- [5] W. A. Benalcazar, T. Li, and T. L. Hughes, *Phys. Rev. B* **99**, 245151 (2019).

- [6] F. Liu, H.-Y. Deng, and K. Wakabayashi, *Phys. Rev. Lett.* **122**, 086804 (2019).
- [7] Z. Wang, B. J. Wieder, J. Li, B. Yan, and B. A. Bernevig, *Phys. Rev. Lett.* **123**, 186401 (2019).
- [8] Y. Tokura, K. Yasuda, and A. Tsukazaki, *Nat. Rev. Phys.* **1**, 126 (2019).
- [9] C.-Z. Chang, C.-X. Liu, and A. H. MacDonald, *Rev. Mod. Phys.* **95**, 011002 (2023).
- [10] L. Šmejkal, Y. Mokrousov, B. Yan, and A. H. MacDonald, *Nat. Phys.* **14**, 242 (2018).
- [11] C. Yue, Y. Xu, Z. Song, H. Weng, Y.-M. Lu, C. Fang, and X. Dai, *Nat. Phys.* **15**, 577 (2019).
- [12] B. Liu, G. Zhao, Z. Liu, and Z. Wang, *Nano Lett.* **19**, 6492 (2019).
- [13] M. J. Park, Y. Kim, G. Y. Cho, and S. B. Lee, *Phys. Rev. Lett.* **123**, 216803 (2019).
- [14] Y. Xu, Z. Song, Z. Wang, H. Weng, and X. Dai, *Phys. Rev. Lett.* **122**, 256402 (2019).
- [15] C. Chen, Z. Song, J.-Z. Zhao, Z. Chen, Z.-M. Yu, X.-L. Sheng, and S. A. Yang, *Phys. Rev. Lett.* **125**, 056402 (2020).
- [16] R.-X. Zhang, F. Wu, and S. Das Sarma, *Phys. Rev. Lett.* **124**, 136407 (2020).
- [17] J.-H. Wang, Y.-B. Yang, N. Dai, and Y. Xu, *Phys. Rev. Lett.* **126**, 206404 (2021).
- [18] F. Schindler, Z. Wang, M. G. Vergniory, A. M. Cook, A. Murani, S. Sengupta, A. Y. Kasumov, R. Deblock, S. Jeon, I. Drozdov *et al.*, *Nat. Phys.* **14**, 918 (2018).
- [19] Y.-B. Choi, Y. Xie, C.-Z. Chen, J. Park, S.-B. Song, J. Yoon, B. J. Kim, T. Taniguchi, K. Watanabe, J. Kim *et al.*, *Nat. Mater.* **19**, 974 (2020).
- [20] R. Noguchi, M. Kobayashi, Z. Jiang, K. Kuroda, T. Takahashi, Z. Xu, D. Lee, M. Hirayama, M. Ochi, T. Shirasawa *et al.*, *Nat. Mater.* **20**, 473 (2021).
- [21] M. Ezawa, *Phys. Rev. Lett.* **121**, 116801 (2018).
- [22] X.-L. Sheng, C. Chen, H. Liu, Z. Chen, Z.-M. Yu, Y. X. Zhao, and S. A. Yang, *Phys. Rev. Lett.* **123**, 256402 (2019).
- [23] Y. Ren, Z. Qiao, and Q. Niu, *Phys. Rev. Lett.* **124**, 166804 (2020).
- [24] N. Mao, X. Hu, H. Wang, Y. Dai, B. Huang, Y. Mokrousov, and C. Niu, *Phys. Rev. B* **103**, 195152 (2021).
- [25] R. Li, N. Mao, X. Wu, B. Huang, Y. Dai, and C. Niu, *Nano Lett.* **23**, 91 (2023).
- [26] L. Cai, R. Li, X. Wu, B. Huang, Y. Dai, and C. Niu, *Phys. Rev. B* **107**, 245116 (2023).
- [27] y. n. P. S. Hur, Namjung a, P. A. Sharma, J. Ahn, S. Guha, and S.-W. Cheong, *Nature (London)* **429**, 392 (2004).
- [28] Y. Yang, H. Zong, J. Sun, and X. Ding, *Adv. Mater.* **33**, 2103469 (2021).
- [29] X. Liu, A. P. Pyatakov, and W. Ren, *Phys. Rev. Lett.* **125**, 247601 (2020).
- [30] L. Seixas, A. S. Rodin, A. Carvalho, and A. H. Castro Neto, *Phys. Rev. Lett.* **116**, 206803 (2016).
- [31] J.-Y. Chaudhary, T. Chirac, S. Fusil, V. Garcia, W. Akhtar, J. Tranchida, P. Thibaudeau, I. Gross, C. Blouzon, A. e. Finco *et al.*, *Nat. Mater.* **19**, 386 (2020).
- [32] D. Di Sante, A. Stroppa, P. Jain, and S. Picozzi, *J. Am. Chem. Soc.* **135**, 18126 (2013).
- [33] Y. Gao, M. Wu, and P. Jena, *Nat. Commun.* **12**, 1331 (2021).
- [34] X. Tang and L. Kou, *J. Phys. Chem. Lett.* **10**, 6634 (2019).
- [35] H. Schmid, *Ferroelectrics* **162**, 317 (1994).
- [36] C. Gong, E. M. Kim, Y. Wang, G. Lee, and X. Zhang, *Nat. Commun.* **10**, 2657 (2019).
- [37] W. Eerenstein, N. Mathur, and J. F. Scott, *Nature (London)* **442**, 759 (2006).
- [38] P. Lunkenheimer, J. Muller, S. Krohns, F. Schrettle, A. Loidl, B. Hartmann, and R. Rommel, *Nat. Mater.* **11**, 755 (2012).
- [39] Y. S. Oh, S. Artyukhin, J. J. Yang, V. Zapf, J. W. Kim, D. Vanderbilt, and S.-W. Cheong, *Nat. Commun.* **5**, 3201 (2014).
- [40] N. A. Spaldin and M. Fiebig, *Science* **309**, 391 (2005).
- [41] S. C. Chae, Y. Horibe, D. Y. Jeong, N. Lee, K. Iida, M. Tanimura, and S.-W. Cheong, *Phys. Rev. Lett.* **110**, 167601 (2013).
- [42] E. Plekhanov, P. Barone, D. Di Sante, and S. Picozzi, *Phys. Rev. B* **90**, 161108(R) (2014).
- [43] S. Liu, Y. Kim, L. Z. Tan, and A. M. Rappe, *Nano Lett.* **16**, 1663 (2016).
- [44] A. Narayan, *Phys. Rev. B* **92**, 220101(R) (2015).
- [45] H. Bai, X. Wang, W. Wu, P. He, Z. Xu, S. A. Yang, and Y. Lu, *Phys. Rev. B* **102**, 235403 (2020).
- [46] J.-J. Zhang, D. Zhu, and B. I. Yakobson, *Nano Lett.* **21**, 785 (2021).
- [47] X.-W. Zhao, S.-N. Dong, G.-Y. Gao, Z.-X. Xu, M. Xu, J.-M. Yan, W.-Y. Zhao, Y.-K. Liu, S.-Y. Yan, J.-X. Zhang *et al.*, *npj Quantum Mater.* **3**, 52 (2018).
- [48] X.-k. Hu, Z.-x. Pang, C.-w. Zhang, P.-j. Wang, P. Li, and W.-x. Ji, *J. Mater. Chem. C* **7**, 9406 (2019).
- [49] Y. Liang, N. Mao, Y. Dai, L. Kou, B. Huang, and Y. Ma, *NPJ Comput. Mater.* **7**, 172 (2021).
- [50] B. Monserrat, J. W. Bennett, K. M. Rabe, and D. Vanderbilt, *Phys. Rev. Lett.* **119**, 036802 (2017).
- [51] Y. Ma, L. Kou, B. Huang, Y. Dai, and T. Heine, *Phys. Rev. B* **98**, 085420 (2018).
- [52] X. Xu, T. Zhang, Y. Dai, B. Huang, and Y. Ma, *Phys. Rev. B* **106**, 205307 (2022).
- [53] G. Kresse and J. Hafner, *Phys. Rev. B* **47**, 558 (1993).
- [54] G. Kresse and J. Furthmüller, *Phys. Rev. B* **54**, 11169 (1996).
- [55] J. P. Perdew, K. Burke, and M. Ernzerhof, *Phys. Rev. Lett.* **77**, 3865 (1996).
- [56] S. Shen, X. Xu, B. Huang, L. Kou, Y. Dai, and Y. Ma, *Phys. Rev. B* **103**, 144101 (2021).
- [57] C. Tang, L. Zhang, S. Sanvito, and A. Du, *J. Am. Chem. Soc.* **145**, 2485 (2023).
- [58] F. Freimuth, Y. Mokrousov, D. Wortmann, S. Heinze, and S. Blügel, *Phys. Rev. B* **78**, 035120 (2008).
- [59] Y. Song, Y. Cao, J. Wang, Y.-N. Zhou, F. Fang, Y. Li, S.-P. Gao, Q.-F. Gu, L. Hu, and D. Sun, *ACS Appl. Mater. Interfaces* **8**, 21334 (2016).
- [60] See Supplemental Material at <http://link.aps.org/supplemental/10.1103/PhysRevB.109.165308> for spatial spin density, energy spectra, and wave function distributions of additional first-principles results for γ -FeO₂H and 1T'-CrCoS₄ monolayers.
- [61] J. Kanamori, *J. Phys. Chem. Solids* **10**, 87 (1959).
- [62] F. Zhang, Y.-C. Kong, R. Pang, L. Hu, P.-L. Gong, X.-Q. Shi, and Z.-K. Tang, *New J. Phys.* **21**, 053033 (2019).
- [63] Y. Bai, N. Mao, R. Li, Y. Dai, B. Huang, and C. Niu, *Small* **19**, 2206574 (2023).
- [64] M. Wu and X. C. Zeng, *Nano Lett.* **16**, 3236 (2016).
- [65] T. Zhang, Y. Ma, X. Xu, C. Lei, B. Huang, and Y. Dai, *J. Phys. Chem. Lett.* **11**, 497 (2020).